Watt level continuous-wave laser in silicon photonics

Neetesh Singh ✉ (ID) ; Kai Wang (ID) ; Sonia M. Garcia-Blanco; Franz X. Kärtner (ID)

Check for updates

View Online   Export Citation

Articles You May Be Interested In

Supercontinuum generation in silicon Bragg grating waveguide

Appl. Phys. Lett. (February 2021)

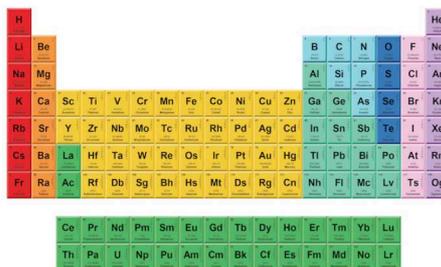Synchronizing Hindmarsh–Rose neurons over Newman–Watts networks

Chaos (July 2009)

Design and performance analysis of gas laser CNC machine CO_2 40 watt

AIP Conf. Proc. (July 2025)

AIP Publishing

Watt level continuous-wave laser in silicon photonics

View Online   Export Citation   CrossMark

Neetesh Singh,[1,a)] (ID) Kai Wang,[2] (ID) Sonia M. Garcia-Blanco,[2] and Franz X. Kärtner[1,3] (ID)

AFFILIATIONS

[1] Center for Free-Electron Laser Science CFEL, Deutsches Elektronen-Synchrotron DESY, Hamburg, Germany
[2] Integrated Optical Systems, MESA+ Institute for Nanotechnology, University of Twente, 7500AE Enschede, The Netherlands
[3] Department of Physics, Universität Hamburg, Jungiusstr. 9, 20355 Hamburg, Germany

[a)] Author to whom correspondence should be addressed: neetesh.singh@desy.de

ABSTRACT

High power sources are desired in integrated photonics to utilize their full potential for various applications such as in telecom, medical, and remote sensing. However, the signal power from the integrated photonic sources has been quite limited. One of the main reasons for this is the usage of small optical mode area waveguides, which, although they help in keeping the footprint small and increasing the gain efficiency, limit the energy storage and extraction capability of the signal from an integrated device, thus limiting the output power. By increasing the optical mode area, one allows the photons to interact with a significantly larger number of gain ions, allowing large energy storage and power extraction. In light of this, we show a high-power continuous wave laser based on a recently demonstrated large-mode-area gain waveguide, which requires no external amplifier. The maximum power generated from the distributed Bragg reflector laser is close to 1.35 W with a slope efficiency of more than 50%, and it operates around the long wavelength window (~1.85 μm) relevant for medical, space, and defense applications. The power level demonstrated here enables silicon photonics based continuous wave light sources comparable to their benchtop counterparts and brings them significantly closer to mass production and deployment for desired applications.

INTRODUCTION

High power lasers are needed in integrated photonics for various commercial and scientific applications. For example, in space communication, high power lasers are required,[1,2] and in telecom/datacom, to compensate for insertion losses due to various components, high power sources are required[3,4] (which is true for even longer wavelengths that can potentially help increase the channel capacity[5–8]). In the long wavelength window, such as near 2 μm, due to strong water absorption, high power lasers find applications in medical surgeries as well as greenhouse gas monitoring on Earth and in deep-space.[9–11] Moreover, the next generation of gravitational wave detectors based on silicon mirrors requires long wavelength lasers to reduce the impact of thermal noise.[12] However, as mentioned earlier, a conventional integrated photonics laser has been limited in output power. Optically pumped lasers, such as those based on rare-earth gain media, are relatively stable against thermal instabilities and nonlinearities such as free carrier absorption and dispersion (compared to semiconductor gain media) and allow for

low noise signal generation owing to the fact they are independent of their host environment (due to lanthanide contraction). The benefits of rare-earth gain were recognized several decades ago, which, for example, led to the development of low noise fiber amplifiers for inter- and intra-continental telecommunication links.[13] Following in the footsteps of bulk systems, the integration of rare-earth in miniature planar devices was pursued (attempts were even made to incorporate rare-earth into the semiconductor hosts).[14,15] However, even though high quality platforms were developed,[16–18] it was hard to implement rare-earth gain in devices in such platforms, which have complex functionalities and are compact and could be mass produced. Over the last decade, rare-earth gain (and even semiconductor gain) has been integrated satisfactorily on the silicon photonics platform.[19–25] However, both semiconductor and rare-earth gain based integrated lasers have struggled to achieve high output power.

One approach that was recognized to increase the output power[26] was to increase the optical mode area (while keeping a large overlap between the gain region and the optical mode), i.e., using a

08 September 2025 10:29:39

large-mode-area (LMA). LMA helps to increase the energy storage of the system and increases the gain saturation power, which is given as $P_{sat} = E_{sat}/\tau_l$, where τ_l is the upper state lifetime and E_{sat} is the saturation energy of the gain medium, which is given as $E_{sat} = \frac{h\nu A_{eff}}{\sigma_{em}+\sigma_{abs}}$, where A_{eff} *is the optical* mode area, $h\nu$ is the photon energy, and σ_{em} and σ_{abs} are emission and absorption cross sections, respectively. The output of a laser or amplifier is directly proportional to both P_{sat} *and the gain. The* gain itself depends on the emission cross section (σ_{em}), the active path length, and the concentration of the gain ion. Typically, the gain is primarily determined by the ion concentration (in the case of fixed path length), which is limited by the maximum concentration a host medium can support without experiencing concentration quenching. Since σ_{em} is an intrinsic property of the rare-earth ion and difficult to modify, P_{sat} becomes the key parameter for increasing output power, which is directly proportional to the mode area A_{eff}. LMA designs also offer additional benefits: they reduce optical nonlinearities, shorten the required length to achieve a given gain, and suppress the rapid buildup of amplified spontaneous emission—common issues in small mode area devices.[27,28] Recently, we have demonstrated a large mode area gain section in silicon photonics to allow large energy storage and its extraction and experimentally demonstrated high energy pulse generation, high saturation power, and watt level output power.[29–32]

In this work, we demonstrate a continuous wave (CW) distributed Bragg reflector (DBR) laser with watt level output power. We have achieved close to 1.35 W of output power at 1.857 μm wavelength. The measured slope efficiency of the laser is over 50%, and the device footprint is ~1.8 mm^2 (0.08 × 22 mm^2). The laser can also be continuously tuned by about 0.5 nm by pump power variation via the thermo-optic effect (with very little change in the spectral shape). The LMA gain medium used has an approximate mode area of 21 μm^2 [limited by the thickness of the gain film deposited with a radio frequency (RF) sputtering tool], and the device only supports fundamental mode operation, which is fully confined in the silicon nitride layer near the input and output of the device. This can facilitate seamless integration of various integrated photonic components

with the laser, which is not possible with fiber or bulk solid-state systems without incurring large losses and size.

DESIGN AND RESULTS

The DBR laser consists of an LMA gain section and two Bragg gratings with high (HR) and low reflectivity (LR), as shown in Fig. 1. In order to avoid etching of the gain layer (unlike in a rib geometry) and have a compact footprint, we implement a layer of another material under the gain layer (such as silicon nitride) to obtain large optical modes.[26] Specifically, the LMA section is defined by a silicon nitride layer (SiN), an interlayer oxide layer (g), and a gain layer (in our case alumina doped with rare-earth gain ions). The designed thickness of the gain layer is ~1.1 μm, the interlayer oxide (g) thickness is 420 nm, and the thickness and width of the SiN layer are 400 and 600 nm, respectively. The device operates in the TE mode, with 88% of the signal power in the gain film, 0.3% in the SiN layer, and 2% in the air above the gain layer, while the rest of the power remains in the silica layer (mainly in the interlayer oxide). The calculated mode area for the signal is 21 μm^2, and the pump is 21.3 μm^2, with a pump and signal mode overlap of >99%. The lasing signal propagates between the LMA section and the passive sections (in which the gratings reside) through adiabatic hybrid tapers. A hybrid taper is a concatenation of appropriately designed linear tapers, where each linear taper is simulated to have high light transmission into the subsequent taper section (similar hybrid tapers have been designed for fully passive structures to reduce taper length[33]). For the hybrid taper, we have chosen four linear tapers with lengths (width variation) of 0.9 mm (0.6–0.9 μm), 0.3 mm (0.9–1.2 μm), 0.1 mm (1.2–1.5 μm), and 0.1 mm (1.5–2.4 μm). The total simulated transmission through the taper is ~98% in a length of 1.5 mm (varying in width from 0.6 to 2.4 μm), which is slightly higher than a corresponding nonlinear taper (by roughly 1%–2%) and 10% higher than a linear taper (which would have to be significantly longer to achieve similar transmission as a hybrid taper). The mode profiles at different SiN widths and the width of the SiN layer vs length are shown for different tapers in Fig. 1(c).
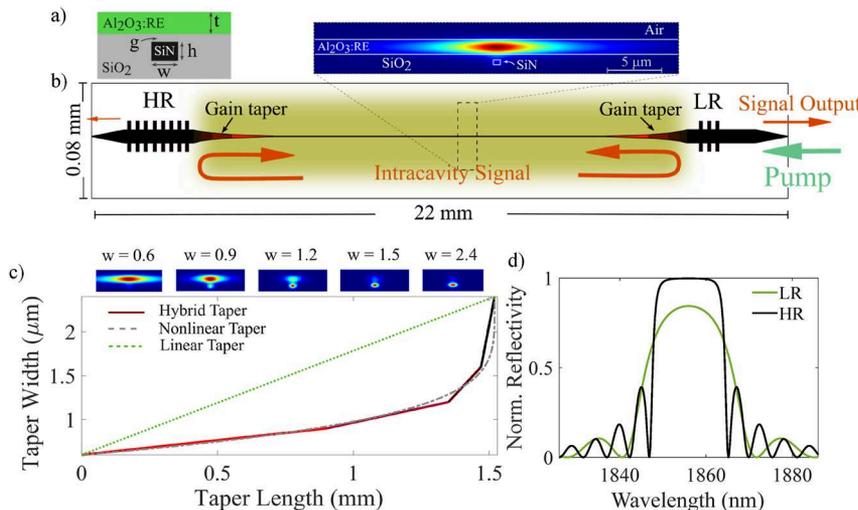
FIG. 1. (a) Device cross section in the LMA region, where t is the gain film thickness, g is the interlayer oxide thickness, and h and w are the height and width of the SiN layer. (b) The DBR laser is pumped, and the signal is collected from the low reflectivity side. (c) The change in width vs length for the hybrid taper (used in this work), nonlinear taper, and linear taper. The mode profiles at different SiN widths (in micrometers) are shown above the plot. (d) The simulated reflection spectrum of the low reflectivity (LR) and high reflectivity (HR) Bragg gratings.

Not only does a hybrid taper show higher transmission, but it is also easier to fabricate when compared to a nonlinear taper in which the steep curvature near the wide SiN region can be difficult if not impossible to fabricate while maintaining a smooth transition. Moreover, an optical mode in a hybrid taper remains mostly in the gain layer for a substantial length of the taper compared to a linear taper. For example, at a taper length of 0.9 mm (from the LMA side), the width of the SiN layer in the hybrid taper is 0.9 μm, which has 81% of optical power in the gain layer, whereas for a linear taper for the same length, the SiN width is 1.7 μm (having only 26% of optical power in the gain layer). As mentioned earlier, the cavity has two gratings—LR and HR. The LR grating side has a peak reflectivity of around 80%, whereas the HR grating has a peak reflectivity of around 98% [see Fig. 1(d)]. The two gratings and the inverse taper input/output couplers are fully clad in silica, so the modes are well confined within the SiN layer.

The device was fabricated in a silicon photonics foundry (LIGENTEC) and subsequently coated with a gain layer in-house. First, a SiN layer is deposited up to a thickness of 400 nm on an oxidized silicon substrate (4 μm bottom oxide), which is patterned with the right dimension and top cladded with a silica layer, which is subsequently etched down to 420 nm to create a gain window [green box in Fig. 1(b)]. For the gain deposition, a 1.1 μm thick thulium-doped alumina gain layer (Tm^{3+}:Al$_2$O$_3$) is deposited by radio-frequency (RF) sputtering with an estimated thulium ion concentration of >6.5 × 10^{20} cm^{-3}.

The device was characterized with an experimental setup shown in Fig. 2(a). The pump at a wavelength of 1.61 μm is launched through a lens into a 99:1 fiber based power splitter, which is subsequently connected to a WDM (which splits/combines the lasing signal and the pump). The WDM is spliced to an anti-reflection coated lensed fiber (3 μm spot size), which launches the pump into the device through the LR grating side. Due to high transmission,

the laser light is collected from the LR grating side rather than the HR grating side (~10× lower output power). The lasing signal is monitored on a calibrated OSA with ~11 dB lower power than the total output. The coupling loss for the pump is close to 1.5 dB/facet, and for the signal it is ~3.2 dB/facet. The chip was mounted and clamped onto a metal plate in order to avoid heating and misalignment during coupling, as was performed in Ref. 31. The laser output power as a function of pump input power is shown in Fig. 2(b). The slope efficiency is >50%, and the lasing threshold pump power is around 80 mW. Up to 1350 mW of output power was obtained for an on-chip pump power of 2.7 W. The lasing wavelength is around 1857.2 nm, as shown in Figs. 3(a) and 3(b). The lasing signal bandwidth suggests there are a few longitudinal modes that are oscillating simultaneously, which is expected from a DBR laser. In our laser, there are roughly 7 modes present, which are ~4 GHz apart (matching to the cavity roundtrip length), as was confirmed by an RF spectrum analyzer, corresponding to a laser linewidth of around 0.33 nm. The minimum power difference between the lasing mode and the non-lasing mode, the suppression ratio, is 64 dB, which suggests that the side mode suppression ratio can be high for a single mode laser. The laser spectrum was measured for various pump powers as shown in Fig. 4(a). We observe that the suppression ratio increases and the spectrum shifts to longer wavelengths with pump power. The increase in the suppression ratio with pump power is mainly due to an increase in the lasing signal power and a reduction in the spontaneous emission factor, which is due to a higher population inversion with high pump power, which helps in suppressing the side modes.[34,35] The shift in the lasing wavelength is mainly due to the change in resonant wavelength due to the thermo-optic effect.[36,37] The index variation of the gain layer (where most of the lasing power resides) due to optical heating causes a change in the resonant wavelength (we neglect thermal expansion as it is relatively weaker), which enables a smooth, mode-hop-free wavelength tuning that can be useful for fine tuning the laser.

If we consider the thermo-optic (TO) coefficient of alumina to be ~5 × 10^{-5}/K,[38,39] we expect a temperature change of ~10 °C for a maximum wavelength variation seen for the laser, which is around 0.5 nm. The change in the center wavelength as a function of on-chip pump power (which corresponds to temperature change) is shown in Fig. 4(b), which appears to be linear as expected, as $\frac{\Delta\lambda}{\Delta T} = \frac{dn_{eff}}{dT}\frac{\lambda}{n_g}$, where $\frac{dn_{eff}}{dT}$ is the TO coefficient, n_g is the group index, and ΔT and $\Delta\lambda$ are the temperature change and wavelength shift, respectively. In addition, we observed a slight change in bandwidth as shown in Fig. 4(c). This can be attributed mainly to self-phase-modulation of a temporally varying lasing signal that results from the interference of multiple longitudinal lasing modes.[40–42] Spatial hole burning can also impact laser bandwidth; however, due to a modest 50 pm increase in bandwidth (~4.3 GHz), which is roughly as wide as one free-spectral-range, and the observed continuous increase in bandwidth with power (no step increase, as would be expected in the case of spatial hole burning[43]), we believe spatial hole burning plays a negligible role in increasing the laser bandwidth. The bandwidth of the laser is in the 300–400 pm range due to relatively broadband gratings utilized in the cavity. The reflection bandwidth of the grating can be reduced in order to achieve narrow-band lasing if desired. The RF spectrum analyzer data of the laser taken with
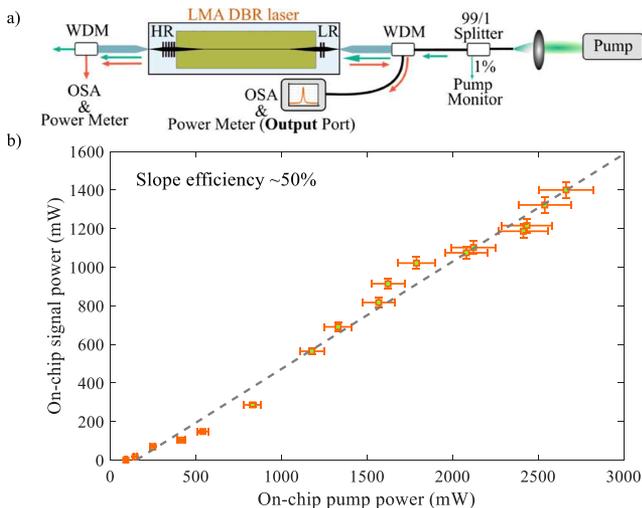

FIG. 2. (a) Experimental setup. WDM—wavelength division multiplexer, LR, HR—low and high reflectivity grating, OSA—optical spectrum analyzer. Pump and signal are shown in blue and red arrows, respectively. (b) On-chip signal power vs on-chip pump power. The error bars represent coupling loss variation.
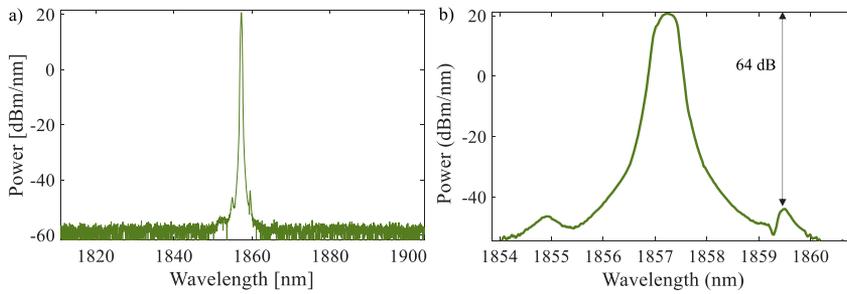
FIG. 3. (a) The optical spectrum of the lasing mode taken over a wide bandwidth, and (b) a close-up showing the minimum power difference between the lasing and the non-lasing mode.
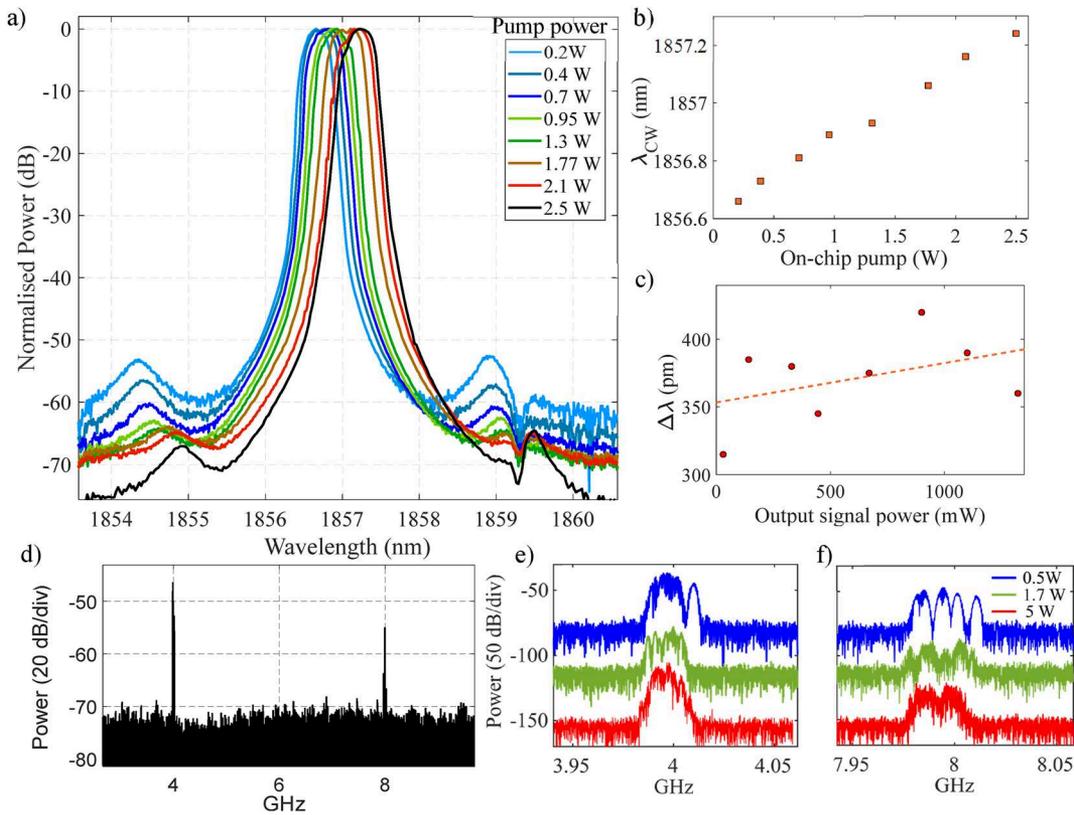

FIG. 4. (a) Pump power dependent laser spectrum. (b) Center wavelength shift as a function of pump power. (c) 3 dB bandwidth of the laser increases with output signal power. (d) RF beat notes of the lasing modes, and (e) and (f) zoomed in RF spectrum around 4 and 8 GHz taken at different pump powers. The spectra are shifted vertically for ease of visualization.

a 12 GHz detector are shown in Fig. 4(d), where we observe the beating of the longitudinal modes, which are spectrally apart from each other by the cavity free-spectral-range (4 GHz). The zoomed-in traces are shown in Figs. 4(e) and 4(f) for different pump power levels.

In conclusion, we have demonstrated a high-power CW laser based on large mode area technology on a silicon photonic platform. Watt-level output power from a mm scale device is shown with a high conversion efficiency. The power can be increased further with the help of an even larger mode, which was limited to ~21 μm^2 in this work by the film deposition tool and improvements in gain film quality. Although the aim of this work was to have high output

power, the linewidth of the laser can also be narrowed for desired applications by implementing gratings with very narrow reflection bandwidths in the cavity, or ultra-narrow linewidths can be achieved with a distributed feedback (DFB) laser cavity (albeit most likely with slightly lower power than what is shown here). The laser output can be launched into free space or a fiber for accessing the laser for components off the chip, or the laser light can be routed to other seamlessly co-integrated photonics components within the same chip for further processing for any desired applications. The fine-tuning capability shown here may find applications, for example, in aligning laser light to a resonator mode or to a specific absorption line for spectroscopic applications, and it can also be used for remote

sensing applications with differential absorption LIDAR for water vapor and carbon dioxide detection and mapping.[44,45] The device was fabricated on a standard 400 nm silicon nitride platform, which is widely available in silicon photonics foundries, which makes the device mass producible and widely deployable.

SUPPLEMENTARY MATERIAL

The long term stability test is reported in the supplementary material.

ACKNOWLEDGMENTS

AUTHOR DECLARATIONS

Conflict of Interest

The authors have no conflicts to disclose.

Author Contributions

Neetesh Singh: Conceptualization (lead); Data curation (lead); Funding acquisition (equal); Investigation (lead); Writing – original draft (lead). **Kai Wang**: Resources (equal). **Sonia M. Garcia-Blanco**: Resources (equal). **Franz X. Kärtner**: Funding acquisition (lead); Resources (equal); Supervision (equal); Writing – review & editing (equal).

DATA AVAILABILITY

All the relevant code and data supporting this study are available from the corresponding author on reasonable request.

REFERENCES

[1]H. Hemmati et al., "Deep-space optical communications: Future perspectives and applications," Proc. IEEE **99**, 2020 (2011).

[2]J. M. Dailey et al., "High output power laser transmitter for high efficiency deep space optical communications," Proc. SPIE **10910**, 109100M (2019).

[3]M. Tan et al., "Co-packaged optics (CPO): Status, challenges, and solutions," Front. Optoelectron. **16**, 1 (2023).

[4]W. J. Zhou et al., "High power CW laser for co-packaged optics," in Conference on Lasers and Electro-Optics (IEEE, San Jose, 2022), pp. 1–2.

[5]Z. Li et al., "Thulium-doped fiber amplifier for optical communications at 2 μm," Opt. Express **21**, 9289 (2013).

[6]P. J. Winzer et al., "Fiber-optic transmission and networking: The previous 20 and the next 20 years [invited]," Opt. Express **26**, 24190 (2018).

[7]R. Soref, "Enabling 2 μm communications," Nat. Photonics **9**, 358 (2015).

[8]Y. Chen et al., "Multi-kilometer long, longitudinally uniform hollow core photonic bandgap fibers for broadband low latency data transmission," J. Lightwave Technol. **34**, 104–113 (2016).

[9]L. Sandström, S. Bäckström, H. Ahlberg, S. Höjer, and A. G. Larsson, "Gas monitoring using semiconductor lasers operating in the 2 μm wavelength region," Infrared Phys. Technol. **39**, 69–75 (1998).

[10]M. Storm, H. Cao, M. Albert, and D. Engin, "Cubesat lidar concepts for ranging, topology, sample capture, surface, and atmospheric science," in Proceedings of the Small Satellite Conference (DigitalCommons, 2017), pp. 5–10, see https://digitalcommons.usu.edu/smallsat/2017/all2017/250/.

[11]N. M. Fried and P. B. Irby, "Advances in laser technology and fibre-optic delivery systems in lithotripsy," Nat. Rev. Urol. **15**, 563–573 (2018).

[12]D. P. Kapasi et al., "Tunable narrow-linewidth laser at 2 μm wavelength for gravitational wave detector research," Opt. Express **28**, 3280–3288 (2020).

[13]R. J. Mears et al., "Low-noise erbium-doped fibre amplifier operating at 1.54 μm," Electron. Lett. **23**, 1026–1028 (1987).

[14]H. Ennen et al., "1.54-μm luminescence of erbium-implanted III–V semiconductors and silicon," Appl. Phys. Lett. **43**, 943–945 (1983).

[15]W. T. Tsang and R. A. Logan, "Observation of enhanced single longitudinal mode operation in 1.5-μm GaInAsP erbium-doped semiconductor injection lasers," Appl. Phys. Lett. **49**, 1686–1688 (1986).

[16]J. I. Mackenzie, "Dielectric solid-state planar waveguide lasers: A review," IEEE J. Sel. Top. Quantum Electron. **13**, 626–637 (2007).

[17]C. Grivas, "Optically pumped planar waveguide lasers, part I: Fundamentals and fabrication techniques," Prog. Quantum Electron. **35**, 159–239 (2011).

[18]K. van Dalfsen et al., "Thulium channel waveguide laser with 16 W of output power and ~80% slope efficiency," Opt. Lett. **39**, 4380–4383 (2014).

[19]Purnawirman et al., "C- and L-band erbium-doped waveguide lasers with wafer-scale silicon nitride cavities," Opt. Lett. **38**, 1760–1762 (2013).

[20]M. Belt et al., "Arrayed narrow linewidth erbium-doped waveguide-distributed feedback lasers on an ultra-low-loss silicon-nitride platform," Opt. Lett. **38**, 4825–4828 (2013).

[21]E. S. Magden et al., "Monolithically-integrated distributed feedback laser compatible with CMOS processing," Opt. Express **25**, 18058–18065 (2017).

[22]N. Li et al., "High-power thulium lasers on a silicon photonics platform," Opt. Lett. **42**, 1181–1184 (2017).

[23]B. L. Segat Frare et al., "On-chip hybrid erbium-doped tellurium oxide–silicon nitride distributed Bragg reflector lasers," Appl. Phys. B **129**, 158 (2023).

[24]Q. Luo et al., "Advances in lithium niobate thin-film lasers and amplifiers: A review," Adv. Photonics **5**, 034002 (2023).

[25]Y. Liu et al., "A fully hybrid integrated erbium-based laser," Nat. Photonics **18**, 829–835 (2024).

[26]N. Singh et al., "Towards CW modelocked laser on chip—A large mode area and NLI for stretched pulse mode locking," Opt. Express **28**, 22562–22579 (2020).

[27]N. G. R. Broderick et al., "Large mode area fibers for high power applications," Opt. Fiber Technol. **5**, 185–196 (1999).

[28]C. C. Ranaud et al., "Characteristics of Q-switched cladding-pumped ytterbium-doped fiber lasers with different high-energy fiber designs," IEEE J. Quantum Electron. **37**, 199–206 (2001).

[29]N. Singh et al., "Silicon photonics-based high-energy passively Q-switched laser," Nat. Photonics **18**, 485–491 (2024).

[30]N. Singh et al., "Sub-2W tunable laser based on silicon photonics power amplifier," Light: Sci. Appl. **14**, 18 (2025).

[31]N. Singh et al., "Watt-class silicon photonics-based optical high-power amplifier," Nat. Photonics **19**, 307 (2025).

[32]M. A. Gaafar et al., "Femtosecond pulse amplification on a chip," Nat. Commun. **15**, 8109 (2024).

[33]J. Zou et al., "Short and efficient mode-size converter designed by segmented-stepwise method," Opt. Lett. **39**, 6273 (2014).

[34]T. L. Koch and U. Koren, "Semiconductor laser for coherent optical fiber communications," J. LightWave Technol. **8**, 274 (1990).

[35]D. J. Blumenthal, J. Buus, and M. C. Amann, Tunable Laser Diodes and Related Optical Sources, 2nd ed. (Wiley, 2005), Chap. II.

[36]P. Alipour et al., "Athermal performance in high Q polymer clad silicon microdisk resonators," Opt. Lett. **35**(20), 3462 (2010).

[37]K. Padmaraju and K. Bergman, "Resolving the thermal challenges for silicon microring resonator devices," Nanophotonics **3**, 269 (2014).

[38]S. Wiechmann and J. Müller, "Thermo-optic properties of TiO_2, Ta_2O_5 and Al_2O_3 thin films for integrated optics on silicon," Thin Solid Films **517**, 6847 (2009).

[39] G. N. West *et al.*, "Low-loss integrated photonics for the blue and ultraviolet regime," APL Photonics **4**, 026101 (2019).

[40] V. Roy *et al.*, "Nonlinear wave mixing in a multilongitudinal-mode erbium-doped fiber laser," Opt. Express **13**, 6791–6797 (2005).

[41] M. A. Lapointe and M. Piche, "Linewidth of high power fiber lasers," Proc. SPIE **7386**, 73860S (2009).

[42] S. I. Kablukov *et al.*, "Output spectrum of Yb-doped fiber lasers," Opt. Lett. **37**, 2508–2510 (2012).

[43] C. L. Tang *et al.*, "Spectral output and spiking behavior of solid-state lasers," J. Appl. Phys. **34**, 2289–2295 (1963).

[44] M. Stephen *et al.*, "Integrated micro-photonics for remote earth science sensing (impress) lidar," in *Proceedings of IEEE International Geoscience and Remote Sensing Symposium* (IEEE, 2019), Return to Ref. 78 in article.

[45] M. Krainak *et al.*, "Integrated photonics for NASA applications," Proc. SPIE **10899**, 108990F (2019).

08 September 2025 10:29:39